



HAL
open science

Generic low-atmosphere signatures of swirled-anemone jets

Reetika Joshi, Guillaume Aulanier, Alice Radcliffe, Luc Rouppe van der Voort, Etienne Pariat, Daniel Nóbrega-Siverio, Brigitte Schmieder

► **To cite this version:**

Reetika Joshi, Guillaume Aulanier, Alice Radcliffe, Luc Rouppe van der Voort, Etienne Pariat, et al.. Generic low-atmosphere signatures of swirled-anemone jets. *Astronomy & Astrophysics - A&A*, 2024, 687, pp.A172. 10.1051/0004-6361/202449553 . hal-04685986

HAL Id: hal-04685986

<https://hal.science/hal-04685986v1>

Submitted on 5 Sep 2024







HAL is a multi-disciplinary open access archive for the deposit and dissemination of scientific research documents, whether they are published or not. The documents may come from teaching and research institutions in France or abroad, or from public or private research centers.

L'archive ouverte pluridisciplinaire **HAL**, est destinée au dépôt et à la diffusion de documents scientifiques de niveau recherche, publiés ou non, émanant des établissements d'enseignement et de recherche français ou étrangers, des laboratoires publics ou privés.



Distributed under a Creative Commons Attribution 4.0 International License

Generic low-atmosphere signatures of swirled-anemone jets[★]

Reetika Joshi^{1,2} , Guillaume Aulanier^{3,1} , Alice Radcliffe³, Luc Rouppe van der Voort^{1,2} , Etienne Pariat³ ,
Daniel Nóbrega-Siverio^{4,5,1,2} , and Brigitte Schmieder^{6,7,8} 

¹ Rosseland Centre for Solar Physics, University of Oslo, PO Box 1029, Blindern 0315, Oslo, Norway
e-mail: reetika.joshi@astro.uio.no

² Institute of Theoretical Astrophysics, University of Oslo, PO Box 1029, Blindern 0315, Oslo, Norway

³ Sorbonne Université, École Polytechnique, Institut Polytechnique de Paris, Observatoire de Paris – PSL, CNRS, Laboratoire de Physique des Plasmas (LPP), 4 Place Jussieu, 75005 Paris, France

⁴ Instituto de Astrofísica de Canarias, 38205 La Laguna, Tenerife, Spain

⁵ Departamento de Astrofísica, Universidad de La Laguna, 38206 La Laguna, Tenerife, Spain

⁶ LIRA, Observatoire de Paris, Université PSL, CNRS, Sorbonne Université, Université de Paris, 5 Place Jules Janssen, 92195 Meudon, France

⁷ Centre for mathematical Plasma Astrophysics, Dept. of Mathematics, KU Leuven, 3001 Leuven, Belgium

⁸ School of Physics and Astronomy, University of Glasgow, Glasgow G12 8QQ, UK

Received 9 February 2024 / Accepted 19 April 2024

ABSTRACT

Context. Solar jets are collimated plasma flows moving along magnetic field lines and are accelerated at low altitude following magnetic reconnection. Several of them originate from anemone-shaped low-lying arcades, and the most impulsive ones tend to be relatively wider and display untwisting motions.

Aims. We aim to establish typical behaviours and observational signatures in the low atmosphere that can occur in response to the coronal development of such impulsive jets.

Methods. We analysed an observed solar jet associated with a circular flare ribbon using high-resolution observations from SST coordinated with IRIS and SDO. We related specifically identified features with those developing in a generic 3D line-tied numerical simulation of reconnection-driven jets performed with the ARMS code.

Results. We identified three features in the SST observations: the formation of a hook along the circular ribbon, the gradual widening of the jet through the apparent displacement of its kinked edge towards (and not away) from the presumed reconnection site, and the falling back of some of the jet plasma towards a footpoint offset from that of the jet itself. The 3D numerical simulation naturally accounts for these features, which were not imposed a priori. Our analyses allowed us to interpret them in the context of the 3D geometry of the asymmetric swirled-anemone loops and their sequences of reconnection with ambient coronal loops.

Conclusions. Given the relatively simple conditions in which the observed jet occurred, together with the generic nature of the simulation that comprised minimum assumptions, we predict that the specific features that we identified and interpreted are probably typical of every impulsive jet.

Key words. Sun: activity – Sun: chromosphere – Sun: corona – Sun: flares

1. Introduction

Solar jets are collimated plasma ejections observed throughout the solar atmosphere. They have been extensively studied in terms of their morphology, dynamic characteristics, and driving mechanisms since their first detection in the X-ray emission of coronal jets by the Soft X-ray Telescope aboard the Yohkoh satellite in the early 1990s (Shibata et al. 1992, 1996; Schmieder et al. 1995). Jet footpoints are observed along magnetic field inversion lines in case of the flux cancellation process (Chifor et al. 2008; Sterling et al. 2018) or in regions of high current density layers with a high squashing factor (Q) called quasi-separatrix layers (QSL; Démoulin et al. 1996; Joshi et al. 2017). Presently, several reviews have discussed the state of the art of jets using several space satellites and ground-based observations (Raouafi et al. 2016; Shen 2021; Schmieder et al. 2022).

Two morphologically different types of solar jets (“straight” and “blow-out”) were introduced by Moore et al. (2010) using

the Hinode/XRT observations. In these observations, it has been found that in some X-ray jets the jet spire remained narrow and the base appeared dim and inert during the jet eruption process. In contrast to these narrow-spire jets, there were other X-ray jets that evolved with wider spires, and during the eruption, the spire width became comparable to the bright and active jet base. It is believed that the narrow-spire straight jets are generated following the standard jet model proposed by Heyvaerts et al. (1977) and Shibata et al. (1992), hence called “standard jets”. However, in the case of broad-spire jets, the eruption blows out the involved emerging bipole magnetic field and along with it cool chromospheric material and the hot jet ejections. These broad-spire jets are hence named “blowout” jets (for more details: Raouafi et al. 2016). Pariat et al. (2015) showed that the formation of either a standard jet or a blowout jet (which can also be called a helical jet) could be governed by differences in the reconnection mode and rate and by the driving process of the magnetic system.

Jet-like events have been detected in almost all wavelengths available to observers. They are called surges when they are

[★] Movies associated to Fig. 2 are available at <https://www.aanda.org>

observed in absorption in chromospheric spectral lines ($H\alpha$) and are frequently associated with hot jets (see, e.g., [Shibata et al. 1995](#); [Mandrini et al. 2002](#); [Uddin et al. 2012](#); [Joshi et al. 2020a, 2021](#)). Several theoretical models and numerical experiments explain the ejection of cool plasma during the jet eruption phase by the rise of chromospheric plasma around the jet in the emerging magnetic flux model ([Moreno-Insertis et al. 2008](#); [Moreno-Insertis & Galsgaard 2013](#); [Nóbrega-Siverio et al. 2016, 2017](#)).

There is a general consensus on magnetic reconnection being a necessary process for the generation of coronal jets. Magnetic reconnection between an emerging photospheric magnetic field and a pre-existing magnetic field can occur at different spatial scales. Reconnection happening in the solar corona produces high-velocity hot jets (10^6 K) observable in X-ray or extreme ultraviolet (EUV; [Shimojo & Shibata 2000](#)), whereas cooler $H\alpha$ surges can be produced by reconnection occurring at the chromospheric layer ([Shibata et al. 2007](#)) or by a slingshot effect next to the hot jets ([Yokoyama & Shibata 1996](#)). When reconnection takes place between a small emerging bipole with an ambient magnetic field of opposite polarity, it gives birth to an anemone-shaped jet, where an opposite polarity connects to the ambient magnetic field in a way that forms a fan-like shape that is similar to a sea anemone ([Shibata et al. 2007](#); [Nishizuka et al. 2011](#); [Singh et al. 2012](#)).

Magnetic reconnection as a generator of the solar jets has been also explored in several numerical simulations. [Yokoyama & Shibata \(1995\)](#), [Moreno-Insertis et al. \(2008\)](#), and [Török et al. \(2009\)](#) performed numerical simulations based on the magnetic reconnection model to reproduce coronal X-ray jets, which successfully demonstrated the connection between jets and magnetic reconnection. At the reconnection site, the plasma may be accelerated by the propagation of magnetic tension through Alfvén waves. In the absence of strong shear or a twist in the system (typical of 2D simulations), this wave is the direct consequence of the reconnection jet, often referred to as the slingshot effect ([Nóbrega-Siverio et al. 2017](#)). When the initially closed system comprises twisted fields, a torsional Alfvén wave is induced in the newly reconnected field line due to the force imbalance between the twisted and the untwisted parts ([Pariat et al. 2009](#); [Török et al. 2009](#); [Wyper et al. 2016](#)).

In addition to these, the jet plasma can be accelerated by “siphon flow”, due to the pressure difference between the top of the newly open field lines and its closed bottom part ([Scott et al. 2022](#)), and by “evaporation” upflow, due to the additional energy deposition induced by reconnection near the jet footpoint. This increases the internal energy at the bottom of the newly reconnected jet loops, forming a pressure gradient that initiates upflows.

The main aim of our present study is to probe the signatures of reconnection in a wide and impulsive jet. Wide and impulsive jets often show twisting features while moving up to evacuate. We address a few questions in this work, such as whether we can see the observational signatures of these jets in the lower corona and what the response in the low corona is to these kinds of jets, which are very common. We present a jet event with coordinated observations that reveal that the jet originated from a swirled anemone, which is the perfect signature of a large-scale non-potential field as a jet progenitor. We chose this simple case event with only one extended magnetic polarity and no mini-filament signatures at the jet base so that the shear is distributed all over the polarity inversion line (PIL). We compared our observational signatures with a theoretical model to address several inquiries about the development of a jet and the

responses within the lower solar atmosphere to the jet’s eruption. Within these responses, could some of the observed characteristics be generic rather than atypical? We aimed for a simple model where the whole parasitic polarity rotates, and this led us to the model given by [Pariat et al. \(2009\)](#). Our observational event is not fully axisymmetric as this model is, and instead it appears to be slightly asymmetric and inclined. So we kept to the same idea from [Pariat et al. \(2009\)](#) but used an inclined version of the model well explained in [Pariat et al. \(2015\)](#).

The paper is organised as follows: An overview of used instruments and observational features of the jet using multi-instruments are presented in Sect. 2. An introduction to the used model and a comparison with observed features are given in Sect. 3. Finally, the results are discussed in Sect. 4.

2. Observations of the jet event

The jet was observed during a coordinated observing campaign between the Swedish 1-m Solar Telescope (SST; [Scharmer et al. 2003](#)) and the Interface Region Imaging Spectrograph (IRIS; [De Pontieu et al. 2014](#)) in active region (AR) 12080 on June 11, 2014. We also used observations from the Solar Dynamics Observatory (SDO; [Pesnell et al. 2012](#)), including UV and EUV images from the Atmosphere Imaging Assembly (AIA; [Lemen et al. 2012](#)) and photospheric magnetic field maps from the Helioseismic Magnetic Imager (HMI; [Schou et al. 2012](#)). The AR was situated in the south-west part of the solar disc centred at $x = 709''$ and $y = -203''$. We focus on an area with parasitic positive magnetic polarity surrounded with negative polarity, which is the region of interest with a circular flare ribbon and jet formation (see Fig. 1). The AR at the western side of the full disc image of the Sun in panel a is zoomed-in in panel b in the EUV wavelength 304 \AA . The distribution of the magnetic field at the active region’s location is depicted in panel c during the jet’s occurrence. The lower row offers a detailed exploration of the jet region, presenting observations at various wavelengths obtained from different instruments. Details regarding the datasets utilised and the observational event are provided in the following subsections. The process of jet formation and ejection is divided into three stages: the quiet phase, the impulsive phase, and the recovery phase. These phases are described in detail in Sects. 2.2–2.4, respectively.

2.1. Instruments

We used the chromospheric $H\alpha$ observations from the CRISP Imaging SpectroPolarimeter (CRISP; [Scharmer et al. 2008](#)) instrument at the SST. The $H\alpha$ line was sampled at 15 spectral line positions at a temporal cadence of 11.4 s and with a pixel size of $0''.058$. The CRISP data was processed with the Multi-Object Multi-Frame Blind Deconvolution (MOMFBD; [Van Noort et al. 2005](#)) image restoration technique. In addition to the chromospheric observations from CRISP, we included the Si IV transition region observations from the 1400 \AA slit-jaw (SJI) channel from IRIS. The SJI 1400 \AA Si IV images were recorded at an average temporal cadence of 17 s and a pixel size of $0''.166$. The aligned SST and IRIS data were previously analysed by [Carlsson et al. \(2015\)](#) and [Skogsrud et al. \(2016\)](#), and are publicly available ([Roupe van der Voort et al. 2020](#)). The SST data were processed following an early version of the CRISPRED ([de la Cruz Rodríguez et al. 2015](#)) reduction pipeline, which includes Multi-Object Multi-Frame Blind Deconvolution (MOMFBD; [Van Noort et al. 2005](#)) image

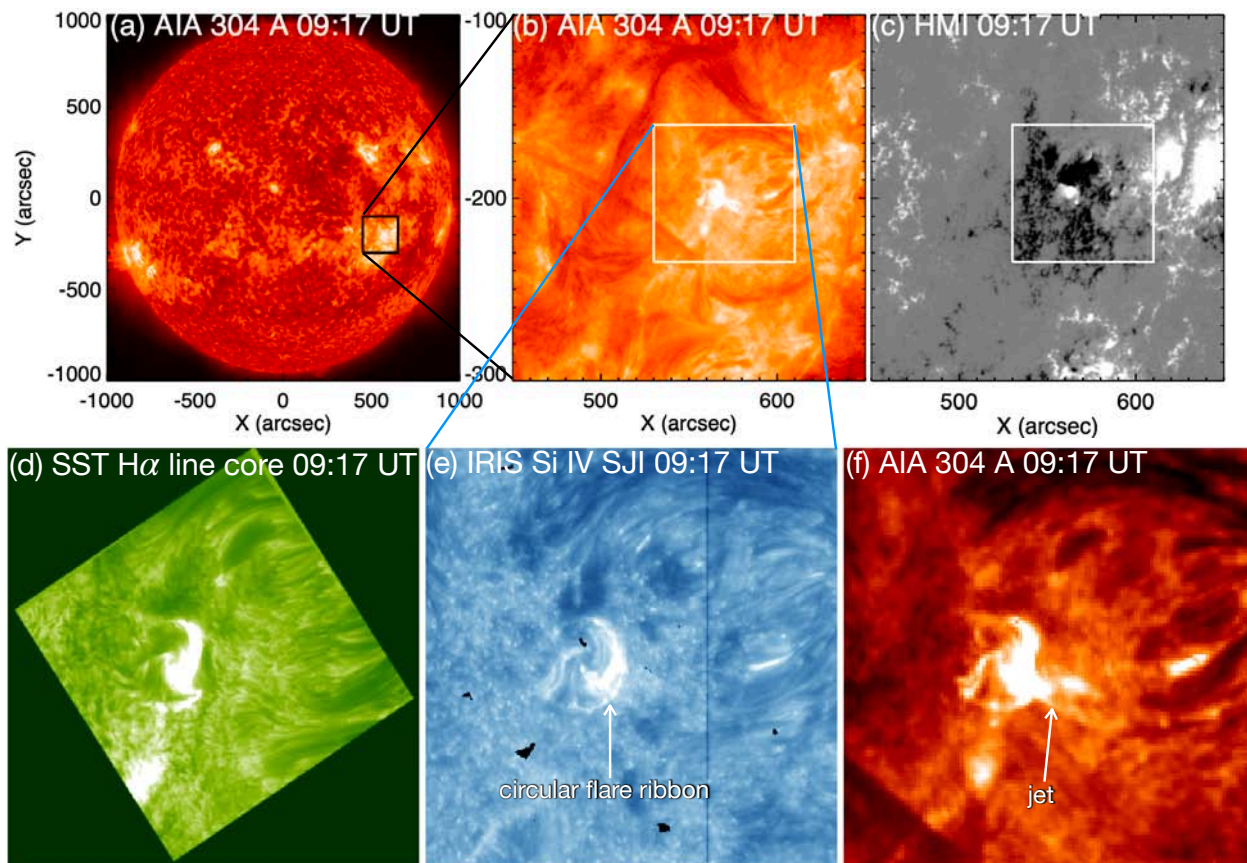


Fig. 1. Multi-instrument observation of a swirled-anemone jet on June 11, 2014, using SDO/AIA, SDO/HMI, SST, and IRIS. Panel a shows the full disc image in AIA 304 Å, with AR NOAA 12080 bounded with a black square. Panels b and c are the zoomed-in views on the AR in AIA 304 Å and line of sight magnetic field. The white rectangular box shows the field of view presented in the bottom row as H α in panel d, Si IV in panel e, and AIA 304 Å.

restoration. For more details on the SST data processing and SST to IRIS alignment, we refer to [Roupe van der Voort et al. \(2020\)](#). These chromospheric and transition region observations were further combined with the AIA 304 Å and 171 Å channels that provide details of the hotter components of the jet eruption. We used one HMI map to show the magnetic field configuration at the jet region, where a small positive polarity patch is embedded inside an extensive area with negative magnetic polarity. The jet region was also scanned through the IRIS slit. However, we do not use the spectral information, as this is beyond the scope of this paper.

2.2. Quiet phase

This AR was a target for coordinated observation with SST and IRIS on June 11, 2014, starting from 07:36 UT, so we examined it for more than an hour before the jet eruption along with the circular solar flare started \sim 09:06 UT. At 08:03 UT, we observed a very clear swirled-anemone structure in the SST H α line core observations and a circular brightening at the same location in the transition region temperature in IRIS Si IV SJIs. When examining the hot temperature EUV channel, interestingly, we observed a straight spine in AIA 171 Å originating from the swirled-anemone base. Figure 2 presents these observational features at 08:03 UT observed with the SDO/AIA, IRIS, and SST instruments. As this straight and narrow spine in the hot EUV channel was observed one hour before the main jet activ-

ity, we refer to it as the quiet-phase jet. In the hot EUV channels, this quiet jet appears at 07:40 UT, disappears after ten minutes, and reappears at 08:02 UT. So this long loop present in the hot EUV channels probably corresponds to some pre-eruptive quasi-steady reconnection ongoing at that location. Its labelling as a jet may be subject to caution, although its relative intermittency may be regarded as being reminiscent of previously-reported hot narrow jets (e.g., some of those seen in [Cirtain et al. 2007](#)).

2.3. Impulsive phase

The swirled-anemone structure observed in the quiet phase started to develop a solar flare at \sim 09:05 UT, and a clear circular flare ribbon formed at \sim 09:16 UT around the anemone-shaped base. Along with the solar flare, a wide solar jet was observed starting at \sim 09:14 UT travelling towards the southwest. The circular flare ribbon formation is evident in the high-resolution IRIS observations (Figs. 3a–c). The jet plasma showed an upward flow in the beginning that was followed by falling-back jet material. From an analysis of the jet H α profiles, we inferred Doppler offsets of about -1.2 Å from the line core, indicating upward velocities around 55 km s $^{-1}$ along the line of sight. Typically, velocities measured in cool jets (surges) are of this magnitude or even smaller, based on both observations (e.g., [Schmieder et al. 1983, 1995](#); [Joshi et al. 2020a](#)) and simulations (e.g., [Moreno-Insertis & Galsgaard 2013](#); [Nóbrega-Siverio et al. 2016](#)).

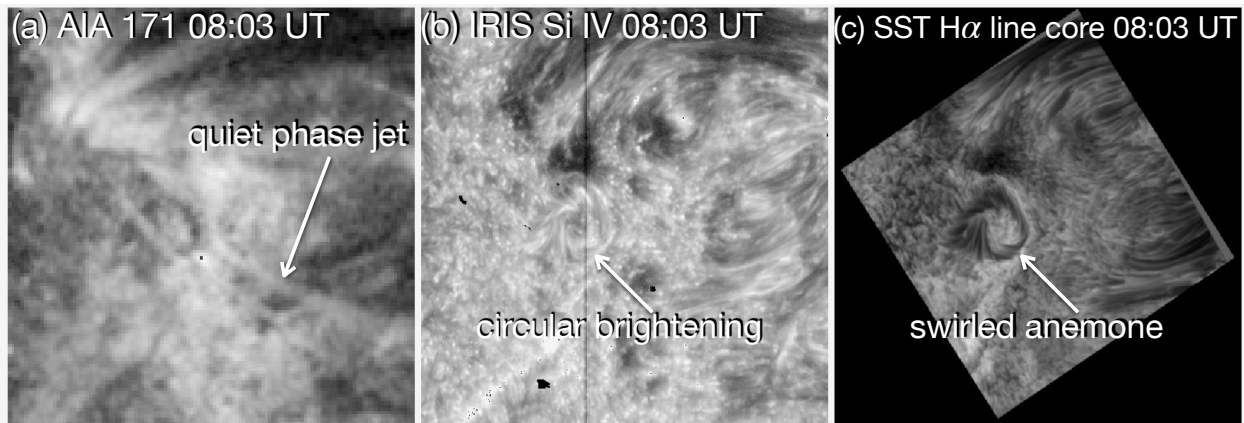


Fig. 2. Quiet phase observations. The quiet or energy storage phase of the jet is shown in AIA 171 Å IRIS Si IV SJI, and in SST H α observations. In the hot AIA channel (panel a), a quiet-phase jet spine is present at 08:03 UT (one hour before the main jet event). The circular brightening is evident in the transition region temperature observed with IRIS (panel b), and the dark absorbed structure of the swirled anemone is observed in the chromospheric H α observations (panel c). The vertical dark line in the IRIS SJI is the position of the slit. The field of view for this figure is presented as a white rectangular box in Figs. 1b and c. This figure has an associated animation that shows the evolution of the region from 08:03 UT to 09:28 UT. Movies are available [online](#).

The H α observations in the red wing ($6563 + 0.4 \text{ \AA}$) were used to probe the downflowing of some of the jet material. With these high-resolution observations, a “hook”-like structure was found to develop in the bright flare ribbon in the north-east of the anemone region (see Fig. 3). This hook structure corresponds to a portion of the flare ribbon. In the standard flare model, the ribbons would be magnetically connected to the reconnection site and would map the footpoint of separatrix field lines (e.g., Savcheva et al. 2015, 2016). A minute or two after, this hook-shaped structure started to deform with time and fade away (Fig. 3, middle row). We highlight this deformation of the hook in Fig. 3 with curved cyan arrows (panels d–f) in H α red wing observations. In the figure, the arrow of the curve is fixed at the north-east side of the hook shape, while the tail of the curve is at the head of the hook. With time, the shorter length of the cyan curve shows the deformation of this hook-shaped structure.

After the deformation of the hook structure, we observed the widening of the jet towards the south in a clockwise direction. An elbow-shaped dark curtain of absorbed plasma material appeared in the H α observations, with a sharp boundary in the south at $\sim 09:18$ UT (see Fig. 3g). It appeared to be moving towards the south in a clockwise direction from $\sim 09:18$ to $09:23$ UT. To reflect the southward motion of this dark plasma (curtain-like structure), we put a straight arrow starting from the elbow of the curtain and heading towards the south in Figs. 3g–i. The arrowhead is fixed in all three panels, and the shortening of the cyan arrows depicts the widening of the jet towards the south with the elbow at the front.

2.4. Recovery phase

Upon inspecting the three different spectral lines of the SST H α observations, blue wing ($6563 - 0.4 \text{ \AA}$), line core (6563 \AA), and red wing ($6563 + 0.4 \text{ \AA}$), we observed that a part of the up-going jet material was falling back during $09:16$ – $09:25$ UT. The origin of the jet from the north of the anemone-shaped base is shown as “jet footpoint” in Fig. 4 along with the wide jet in the blue wing. Strong absorption in the blue and red wings of the H α wavelength revealed that the plasma material was being propelled upwards (blueshifted) as well as downwards (redshifted). It is not necessarily the same plasma material that was flowing up and

down. It is interesting to notice that the jet material was falling back at an offset location in the anti-clockwise direction from the jet footpoint. The observations give an idea that the falling-back jet material follows a different path than the upflow plasma material. Figure 4 illustrates this scenario with a time evolution of the jet flow in three different spectral lines next to each other. Panel i in the figure presents the offset between the jet footpoint and the return footpoint.

3. Modelling versus observed features

The observed wide jet with an anemone-shaped base in the parasitic magnetic topology resembles the generic jet model of Pariat et al. (2015, see their Fig. 1). In the following, we explain the main features of the original model developed by Pariat et al. (2015) and the variations we apply in this paper to that model in Sect. 3.1, comparing the results from this numerical experiment with the observational features.

3.1. ARMS simulation and QSL calculation

The model used to obtain insights on the dynamics of the observed jet is based on the numerical experiments of Pariat et al. (2015) performed with the Adaptively Refined MHD Solver (ARMS) numerical code (DeVore 1991). Complete information about the ARMS code and the setup of the numerical experiment can be found in Pariat et al. (2015, and references therein). The concepts for this 3D model for solar jets were initially proposed by Pariat et al. (2009) and have been developed since then in multiple directions (e.g., Pariat et al. 2010, 2015, 2016; Dalmasse et al. 2012; Wyper et al. 2016, 2018, 2019; Karpen et al. 2017). Comparisons between this model and observations have already been carried out by Patsourakos et al. (2008) in order to understand the 3D properties of coronal jets observed stereoscopically by the EUV imagers of the STEREO mission (Howard et al. 2008).

The fundamental basis of this jet model centres around the presence of a 3D null point, which partitions the coronal volume into two connectivity domains. One domain is closed, situated below the dome-like fan separatrix surface of the null point, while the other domain is open and positioned above

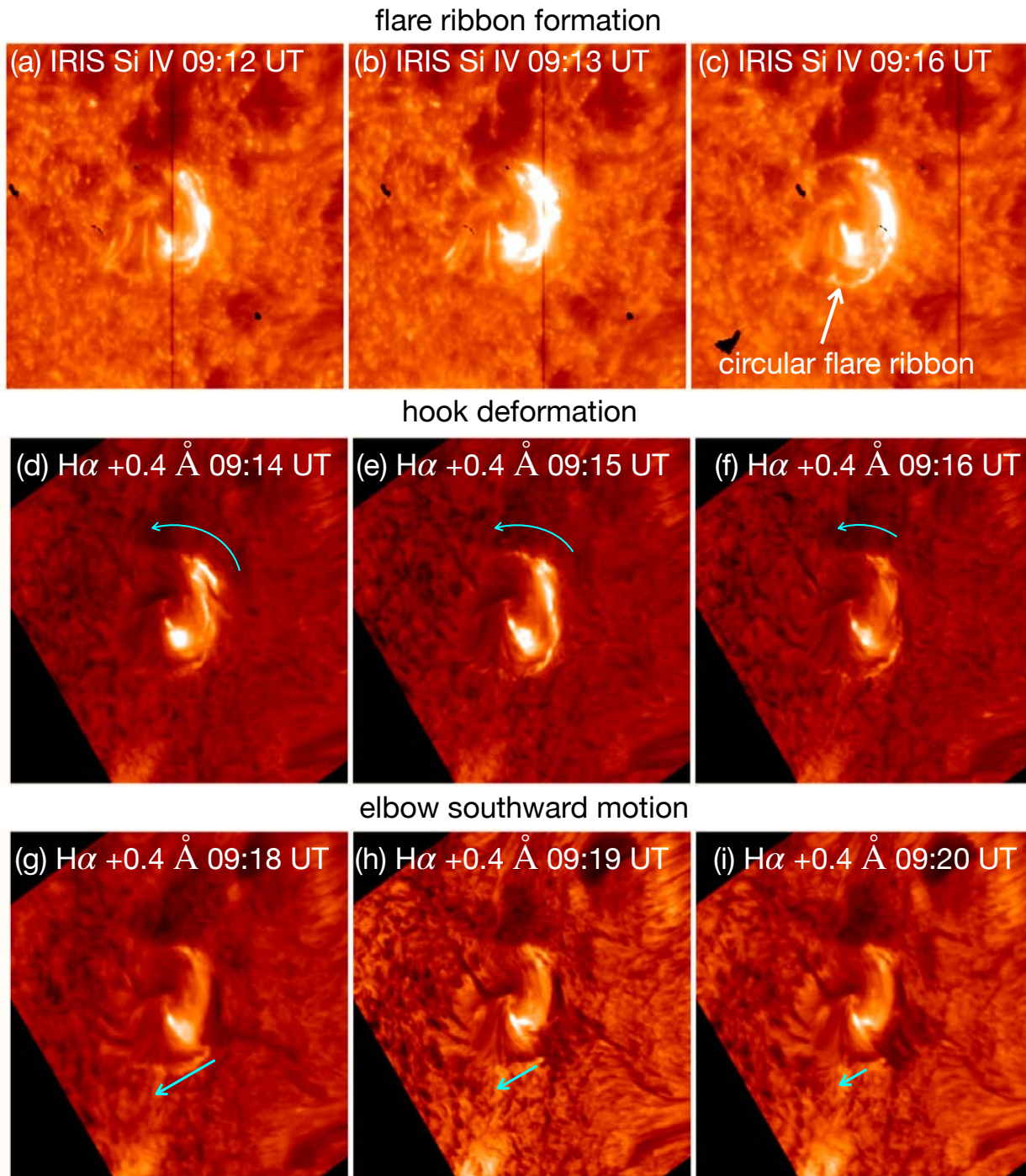


Fig. 3. Impulsive phase observation. This energy release phase is shown in three stages. The top row shows the circular flare ribbon formation in IRIS Si IV observations. The middle row shows the deformation of the hook brightening in the H α red wing and is indicated with curved cyan arrows. The bottom row shows the southward motion of the dark elbow-shaped structure in the H α red wing and is depicted with the shortening of the arrow length.

it. In the simulations, this standard null-point configuration is the result of a vertically oriented magnetic dipole embedded slightly below the bottom boundary, which generated a photospheric magnetic field concentration, and a large-scale nearly uniform, spatially slowly varying background vertical magnetic field with a direction opposite to the dipole. As can be seen in Fig. 5a, the resulting configuration contains two distinct flux systems: a circular patch of strong closed magnetic flux surrounded by weaker open flux. This type of magnetic field config-

uration is very commonly observed with coronal jets and coronal bright points (Moreno-Insertis et al. 2008; Zhang et al. 2012; Joshi et al. 2017; Nóbrega-Siverio et al. 2023).

The numerical simulation analysed in the present study is a variation of the parametric simulations presented in Pariat et al. (2015), for which the uniform background vertical field was inclined by 30°. More precisely, the magnetic field was defined by Eq. (2) of Pariat et al. (2015) with the angle θ defined by the inclination of the open field with respect to the vertical direction

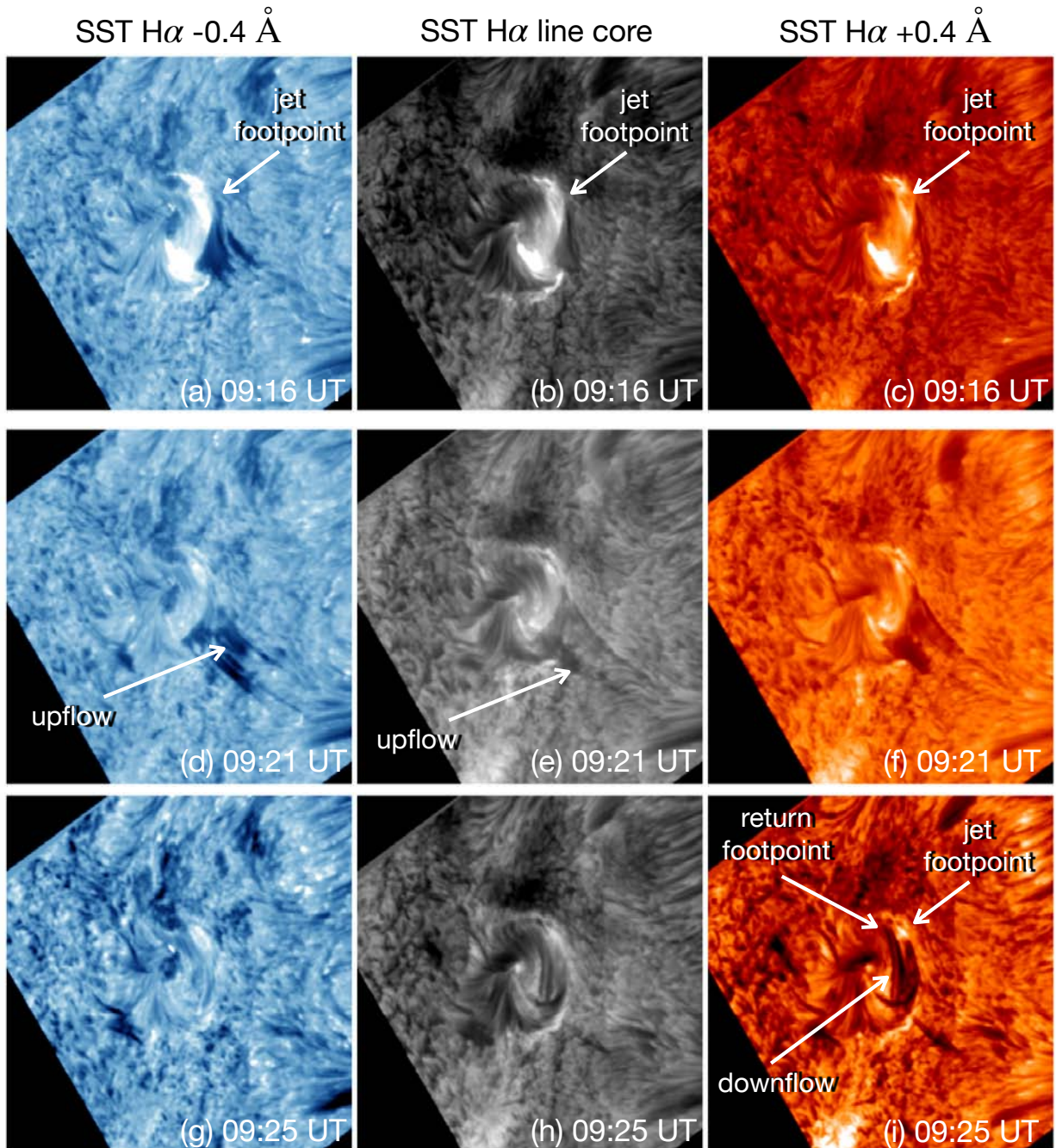


Fig. 4. Recovery phase observation. This is the last phase of the jet eruption. The up- and downflow of the jet plasma is shown in the SST H α blue wing (first column), line core 6563 \AA (middle column), and red wing (last column) observations. The initial jet footpoint is shown in the first row and is where the jet starts to erupt as a wide upflow shown in panels d and e. Some parts of the jet material fell back at a different location: “return footpoint”, shown in panel i.

such that $\theta = 30^\circ$ ($\theta = 0$ would correspond to a vertical field). Such a null-point magnetic topological system permits very efficient storage of magnetic energy in the closed domain, either thanks to shear (e.g., [Pariat et al. 2009](#)) or the formation of a twisted flux rope (e.g., [Wyper et al. 2018](#)). In the present study, the injection of magnetic energy and helicity into the system follows [Pariat et al. \(2015\)](#): very slow (with respect to the local Alfvén speed) horizontal motions were applied at the line-tied photospheric boundary and only in the main central positive of the closed magnetic polarity. The system evolved quasi-steadily, with field lines being slowly sheared above the PIL (see Figs. 5b

and c). As the magnetic system acquired poloidal flux, it slowly bulged, and the fan dome and 3D null point rose. Similarly to [Pariat et al. \(2009\)](#), the driving motions are along the isocontours of the magnetic field. However, unlike with the axisymmetric configuration of [Pariat et al. \(2009\)](#), because of the inclination of the vertical field, the driving motions also became asymmetric. This naturally resulted in asymmetrically sheared field lines, as observed in Fig. 5c. This is reminiscent of the observed “swirled-anemone” feature of the present event and justified the choice of driving used here for the comparison between the observation and the numerical model (cf. also Sect. 3.2).

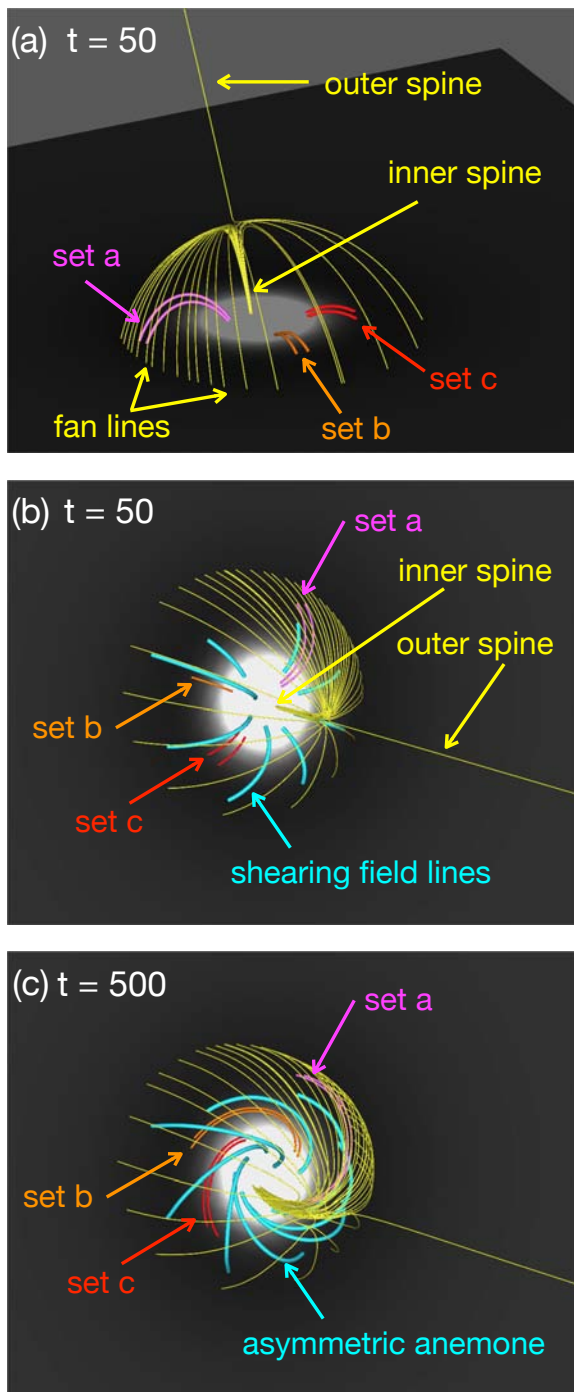


Fig. 5. Initial configuration for the model adapted from [Pariat et al. \(2009\)](#) from a slanted view point (panel a) and a view point that is similar to the observations (panels b and c). The yellow lines graze the separatrices, and the boundary of the white circle in panels b and c acts as the PIL. Shearing magnetic field lines in the beginning phase (panel b) evolve as an asymmetric anemone shape around the PIL (panel c). The different sets of field lines are explained in Sect. 3.1.

Finally, the null-point configuration enabled a very efficient energy release, thanks to magnetic reconnection (e.g., [Pariat et al. 2009, 2010](#)), inducing the self-consistent generation of a complex impulsive solar jet-like eruption, presenting both bulk flows and wave dynamics, being multi-velocity and multi-thermal, similarly to observed jets ([Patsourakos et al. 2008](#);

[Raouafi et al. 2016](#); [Joshi et al. 2020b](#)). The adiabatic energy equation used in the model of [Pariat et al. \(2015\)](#) only permits a limited understanding of the plasma emission and absorption in comparison to more sophisticated numerical experiments ([Fang et al. 2014](#); [González-Avilés et al. 2020](#); [Chen et al. 2022](#)). Nonetheless, in the low beta coronal environment, the model is fully capable of capturing the essential dynamics of magnetic field lines. Of significant importance is the implementation of an adaptive mesh refinement strategy, as detailed in the appendix of [Karpen et al. \(2012\)](#), because it enhances grid resolution at the sites of reconnecting current sheets. This enhancement allows for the precise identification of diffusion regions and the reconnection site. Such an approach enables a confident comparison with observational data, as elaborated in Sect. 3.2.

In addition, in order to analyse and visualise the magnetic topology and the evolution of the magnetic connectivity, we computed the squashing factor Q ([Titov et al. 2002](#); [Titov 2007](#)). The squashing factor is a measure of the gradients of the connectivity mapping between two planes. Numerically, the computation was done following the [Aslanyan et al. \(2021\)](#) implementation of the GPU-compatible QSL Squasher code ([Tassev & Savcheva 2017](#)). More specifically, following [Aslanyan et al. \(2021\)](#), we plotted a modified version of the signed $\log Q$ ($\text{slog } Q$; [Titov et al. 2011](#)) initially introduced by [Titov et al. \(2011\)](#), in which positive and negative values of Q are computed between different couples of reference planes. By applying the red–blue palette to the $\text{slog } Q$ distributions, we were able to simultaneously visualise (quasi-)separatrix footprints for both the open (negative/blue) and closed (positive/red) magnetic fields. One should keep in mind that since the Q values were computed between different planes for the open and closed fields, the absolute Q values do not have the same significance. However, since we are here only interested in the morphology of the Q distribution as well as the dynamics of the separatrix between open and closed field, the $\text{slog } Q$ maps are very instructive, in particular to understand and interpret the observed dynamics of the flare ribbons (see Sect. 3.4).

3.2. Early reconnection and straight jet

In the relatively earlier phase of the simulation, the magnetic shear of the coronal arcades (as induced by the slow rotational boundary motion prescribed in the parasitic positive polarity) resulted in a gradual bulging of the shearing field lines. Given the asymmetric nature of the initial magnetic field configuration, the bulging is actually not axisymmetric around in the inner spine. Indeed, simple geometrical arguments point to the fact that relatively larger shear angles are induced in relatively shorter field lines for the same shearing footpoint displacements. These different shear angles generate relatively stronger Lorentz force imbalances in relatively shorter and more sheared field lines and therefore tend to expand relatively more to find their sheared equilibrium. This eventually results in one section of the fan surface (the one on the left in panel a, being on the right in panel b, in both Figs. 5 and 6) along with its corresponding “set a” of underlying field lines to actually bulge more than any other part of the fan and any other set of field lines. This differential bulging is responsible for the gradual formation of a current sheet around the null point (as manifested by the acute angle made between the fan surface and the spine field line seen in Fig. 6a). This gradual current-sheet formation process due to field-line bulging is actually similar to what happens in simulations of flux emergence on one side of a null point

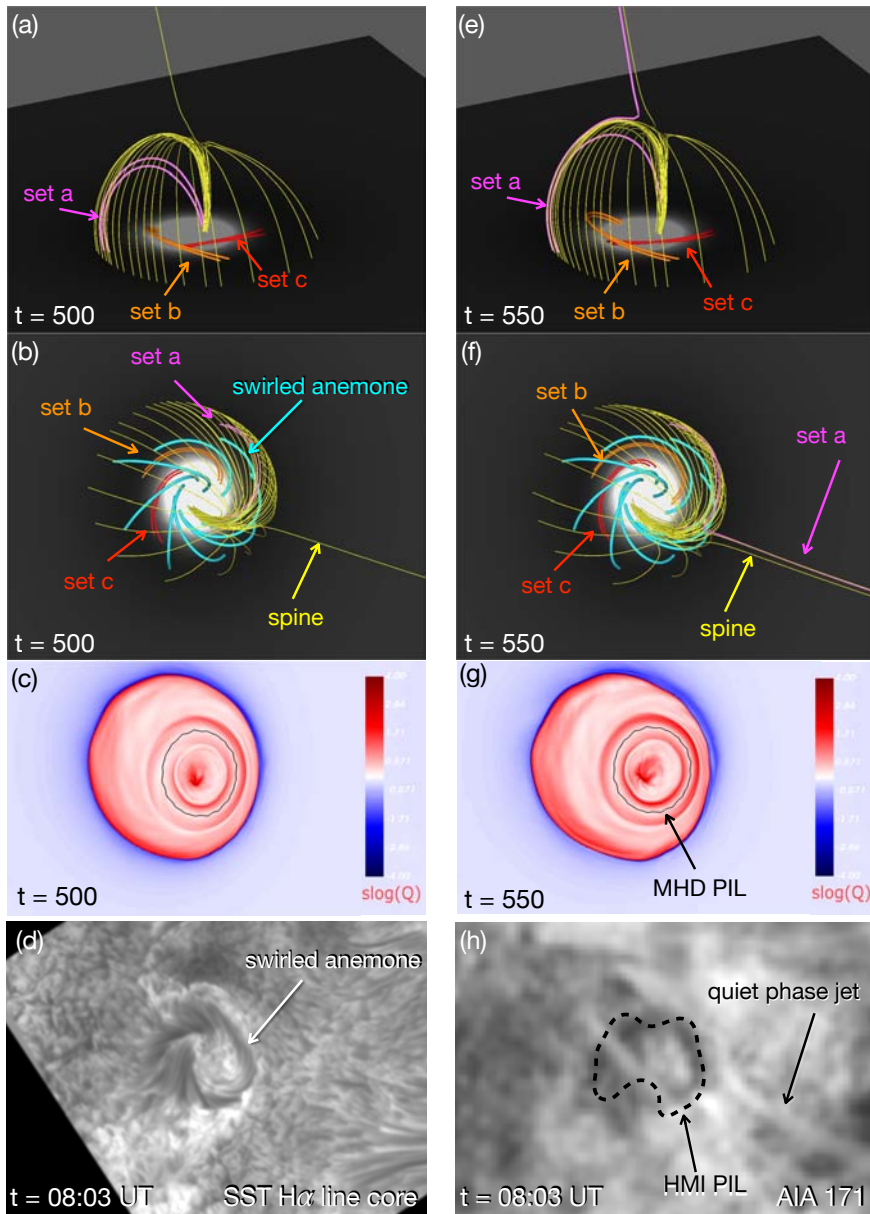


Fig. 6. Modelling versus observations phase I. The rows are as follows: early reconnection phase in the ARMS simulation (first and second row), QSL calculations (third row), and in observations (last row). The first row is the field line view from the side, and the second and third rows have the same orientation as the observations. The swirled-anemone shape in the simulation is shown in panel b around the MHD explained in the QSL map in panel g. The similar shape in observation is shown in the SST $H\alpha$ line core observations (panel d) around the HMI PIL overplotted in AIA 171 Å (panel h).

(e.g., [Moreno-Insertis & Galsgaard 2013](#); [Nóbrega-Siverio et al. 2016](#)).

In the current model, at time $t = 500$, the asymmetric swirled-anemone has evolved into a configuration where its sheared-most field lines (illustrated in cyan in Figs. 5 and 6) are now almost aligned with the PIL, as depicted in Figs. 6a and b. This occurs nearly simultaneously with the current sheet reaching the scale of the mesh in the vicinity of the coronal null point, approximately at $t \approx 550$. This event signals the initiation of magnetic reconnection and the beginning of the jet. Nevertheless, the resulting modelled jet is yet in a relatively quiet stage. Indeed, the reconnection and the plasma dynamics are not very impulsive. They neither involve any large-scale restructuring of magnetic field connectivities nor lead to bulk plasma acceleration at the scale of the whole system. Instead, field lines reconnect gradually in a quasi-two-dimensional way, with little total flux transfer per unit time from below the fan surface to above it along the outer-spine field line. The latter can be seen qualitatively from Fig. 6. Indeed, panels e and f show one of the pair of

“set a” field lines (drawn in pink) that has reconnected between $t = 500$ and $t = 550$, while all the other represented field lines, including the other very close-by “set a” field line, have hardly evolved between these two times. Also, panels c and g show how the footpoints of the QSL have almost rigidly and only slightly shifted (towards the left) during this reconnection, sweeping a relatively small area that contains the footpoint of the single “set a” reconnecting field line.

These signatures are typical of a two-dimensional-like reconnection pattern that does not involve the whole magnetic field configuration. Instead, these manifestations are, as expected, reminiscent of what was already extensively described in [Pariat et al. \(2015\)](#), what they named the “straight jet” phase (illustrated in the left panels of their Fig. 1). Interestingly, it is also at the same time that the swirled anemone and the quiet (straight) jet are seen together in the SST and SDO observations of the event studied in this paper (see Figs. 6d and h). So far, all of these behaviours are typical of non-helical jets (as reviewed in [Raouafi et al. 2016](#)) and of some

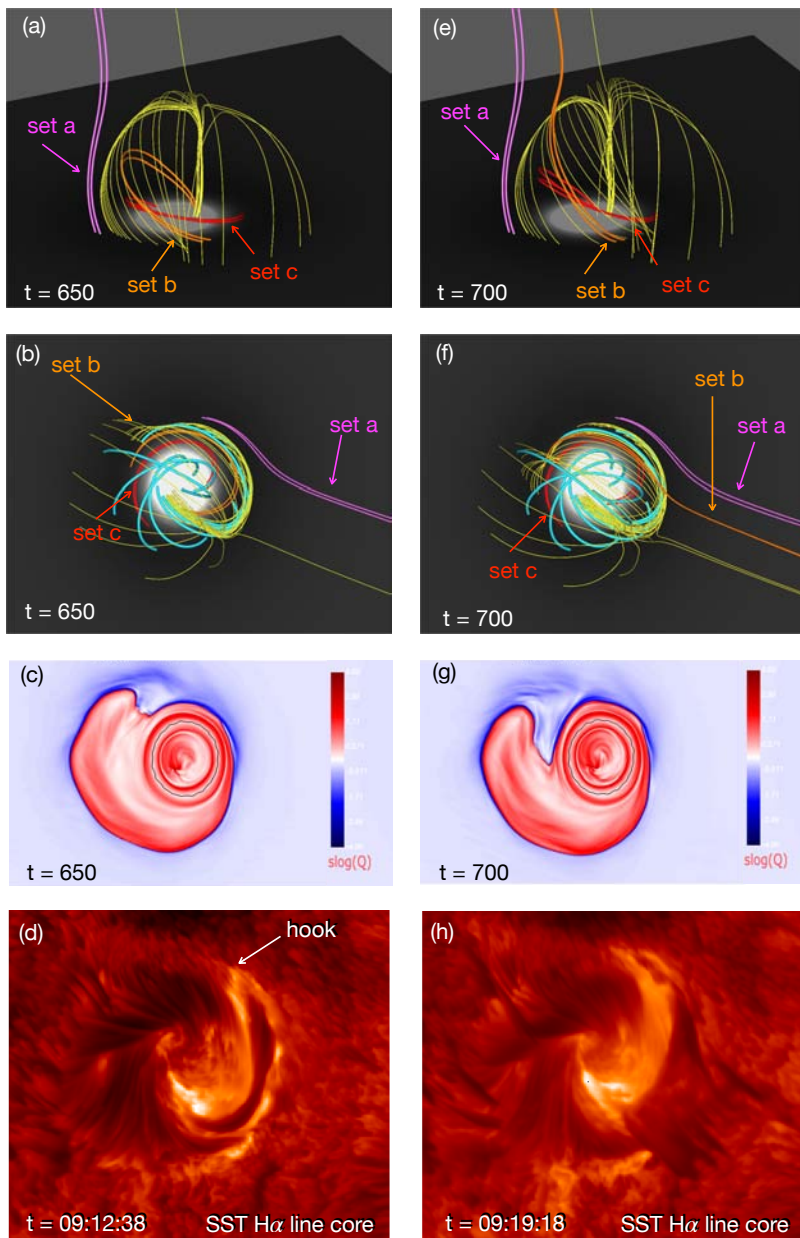


Fig. 7. Modelling versus observations phase II. The rows are as follows: the impulsive phase of the jet in the field line simulation from a side view (first row), an observational view (second row), the squashing factor maps (third row), and SST $H\alpha$ line core observations (last row).

circular-ribbon and null-point related confined flares (see e.g., Masson et al. 2009; Guglielmino et al. 2010; Zuccarello et al. 2017; Prasad et al. 2020; Devi et al. 2020; Cheng et al. 2023). But in the present model, they represent only the precursor of a much more dynamic phase, extensively studied by Pariat et al. (2015), which we subsequently analyze concerning its low-altitude manifestations.

3.3. Fast widening of the jet

By time $t = 650$ – 700 , the system endures a global ideal kink instability and produces a “helical jet”, as described in Pariat et al. (2015). This kink instability first pushes against the fan surface from below, resulting in an extension of the current sheet over a significant fraction of the fan, that is, not only in the vicinity of the null point. Secondly, this extended current sheet provides a widespread region over which magnetic reconnection occurs, involving sheared field lines located at various

places under the fan, and eventually allows the widening of the jet over a transverse scale length comparable to the size of the fan. This widening of the model jet is illustrated in Figs. 7a–f, where the second field line of “set a” (in pink) has reconnected in the time interval $t = 550$ – 650 and both field lines of “set b” (in orange) are reconnecting in the time interval $t = 650$ – 700 . The distance between these field lines, as well as with the outer spine (in yellow), shows the width of the modelled jet.

Upon revisiting our SST observation, it became evident that the studied jet not only widened, resembling a dark curtain, but also extended clockwise towards the south, with its leading edge forming an elbow-like structure (see the cyan arrow in Fig. 3g). This may lead one to think that the jet was extending towards the null point, as it was located at the top of the elbow. Such a behaviour would be puzzling since it would imply that the jet did not extend away from the null point, as post-reconnected relaxing field lines should normally behave. Instead, we conjecture that the elbow of the dark curtain actually marks the position of

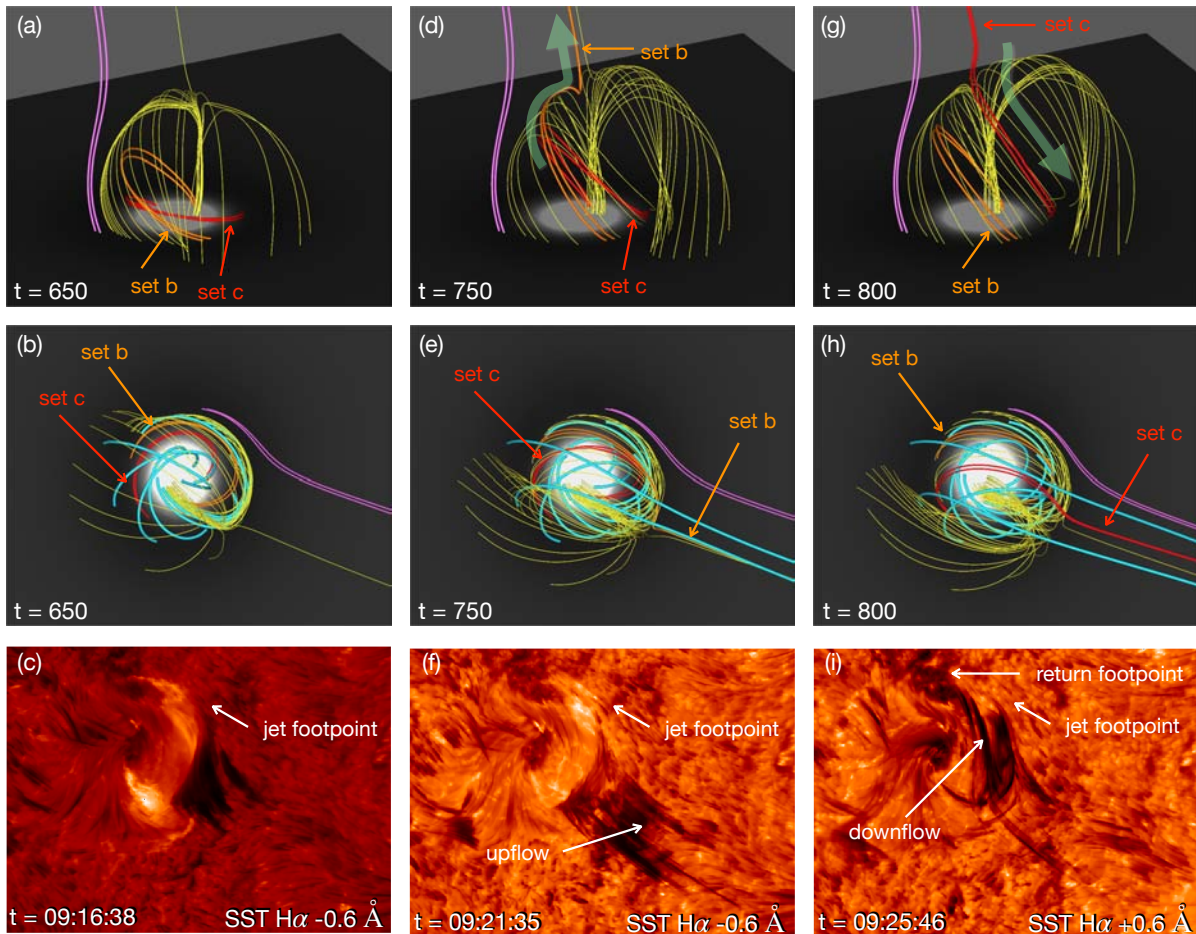


Fig. 8. Modelling versus observations phase III. This was the last stage of the jet eruption, where a part of the jet material fell back on a different footprint than the initial footprint. The first row is the side view of the simulated field lines, the second row is the observational view of the simulation, and the third row presents the H α observations in the blue (panels c, f) and red (panel i) wing. The thick green arrow in panel d shows the direction of the jet upflow along the open set b field lines, and the arrow in panel g shows the downflow of the jet material along the set c field lines.

the null point (or almost). In this line, what SST shows would be a fast shift in position of the null towards the south during the impulsive phase of the jet. However, this shift does not happen in the MHD simulation. On the contrary, a shift in the opposite direction would have even been expected. Indeed, both the magnetic reconnection and the jet itself remove free magnetic energy from below the fan. This energy decrease should force the magnetic configuration back towards the potential field, for which the null point is offset counterclockwise as compared to the jet state (compare Figs. 5 and 7). However, the counterclockwise rotation of the null point does not manifest in the simulation either. We propose that the observed stagnation of the modelled null point may be attributed to the natural counterclockwise rotation resulting from the energy decrease, which must be counterbalanced by a clockwise rotation. This clockwise rotation could potentially be induced by the coupling between the kink instability and reconnection, leading to large-scale rotational motions at the helical jet's base. However, this conjecture requires further quantitative investigation in future studies.

3.4. A hook moving along the circular ribbon

Following the usual association between QSL footprints in models and flare ribbons in observations, the simulation qualitatively

retrieves the occurrence and the displacement of the observed hook-like structure in the circular flare ribbon located at the north-west of the parasitic polarity (see Figs. 3 and 7d, h, for the SST observation). However, this match is only qualitative. Indeed, the hook in the model is rather located at the north-east of the parasitic positive polarity, and it even evolves towards the east (see Figs. 7c and g). Nevertheless, it is interesting to note that this evolution of the circular ribbon is not only very different from the earlier quiet (straight) jet phase described above but also that it was not prescribed a priori in the simulation setup. Instead, this is a behaviour that spontaneously emerged from the free evolution of the system once the photospheric driving was stopped.

This hook-shaped structure in the circular ribbon actually traces the edges; “a channel of locally open field forms, penetrating deep into the previously closed field region as far as the polarity inversion line”, as written by [Wyper & DeVore \(2016\)](#), who obtained the very same behaviour in their jet simulation (plotted in their Fig. 8). This origin and the shift in position of this finite-sized inclusion of reconnected field are difficult to firmly establish, but both seem to be associated with the deformation of the flux tube that surrounds the inner spine while it endures the ideal kink instability. This ongoing coronal deformation of the flux tube would naturally be responsible for a

gradual shift in position of the bulging of the field lines below the fan, even after the photospheric drivers have been switched off, as these field lines are pushed by the kinking inner spine. This relates in a straightforward way to the sequential shifting of reconnection starting with the field lines of “set a” (Fig. 6), moving to those of “set b” (Fig. 7), and eventually involving those of “set c” (Fig. 8).

In this context, the presence and displacement of a hook along the circular flare ribbon illustrates the gradual shift in the positions of coronal kinking, bulging, and reconnection onto the surface. These phenomena are inherent in a swirled-anemone configuration, even in its most basic, generic, and initially symmetric form in [Pariat et al. \(2009\)](#). Furthermore, it is important to highlight that while the moving hooked ribbon correlates with the overarching large-scale swirling or twisting pattern of the system, it does not signify (at least in our simulation) the existence of a drifting low-lying flux rope positioned along the PIL, as hooked ribbons typically do in the context of two-ribbon flares (see [Aulanier & Dudík 2019](#)). Therefore, while the hook remains associated with the presence of some twist, it does not serve as a definitive signature of a flux rope.

3.5. Downflow of the jet plasma offset from its launch site

The last peculiar behaviour that we noticed in this jet was the falling back of some of the jet material at a “return footpoint” located at a position (counterclockwise) different from the “jet footpoint”, the latter corresponding to the launch site of the material from the chromospheric layer (see Fig. 4). On one hand, the simulation does not include gravity, and it uses an initially uniform atmosphere, so it cannot be used to model, plot, and follow the lift-off followed by the fall of chromospheric jet material. On the other hand, one can still use the simulation to follow the spatio-temporal evolution of its field lines and use these lines to infer how some material would flow along the field, according to some gravitational pull towards the line-tied plane. This is how we proceed hereafter.

The field line analysis is reported in Fig. 8. There it can be seen that the field lines from “set b” (in orange) that have reconnected and opened into the jet at $t = 750$ have actually reconnected a second time and have been closing down below the fan surface by $t = 800$. As a consequence, any chromospheric material that could have been accelerated along these “set b” field lines and reached out into the jet at high altitude above the fan by $t = 700$ would have no way of falling back to their initial position along the same “set b” field lines for $t \leq 800$ because those lines would no longer be connected to the jet. Meanwhile, the field lines from “set c” (in red) are shown to be reconnecting and opening into the jet at time $t \approx 800$. These “set c” field lines now provide new channels along which previously accelerated material have the possibility to fall back to the line-tied plane in the model (i.e. the chromosphere in the real Sun). These new “set c” channels have footpoints that are offset from those of the “set b” field lines. When the model is oriented with angles corresponding to projection of the event as observed from Earth (see Figs. 8b, e and h), one can see that this offset of the “set c return footpoints” is counterclockwise from the position of the “set b jet footpoint”.

Interestingly, similar to the observation regarding the hook, this generic and idealised model qualitatively corresponds to the observed behaviour, particularly concerning the offset of the downflowing jet material. Notably, no specific configuration was imposed in the simulation to account for this behaviour. It is also noteworthy that this observed offset, which may be perceived as

complex, differs from the straightforward fallback of material to its point of origin, as the latter is an inherent property of a relatively simplified model.

Finally, it should be emphasised that the model allows one to make a causal association between the moving hook and the offset of the downflowing material away from the jet footpoint. The fact that both are moving counterclockwise along the circular ribbon already provided a first observational hint that they were related. Thanks to the model, we could see that these elements are actually coupled through magnetic reconnection in the corona. The moving hook (see Sect. 3.4) is located on the edge of an equally moving open-field penetrating-region (as first noticed in [Wyper & DeVore 2016](#)), and that is the signature at the low atmospheric level of the coronal reconnection dynamics that close some previously open fields (along which jet plasma was accelerated earlier); open previously closed and distant field lines (along which the same plasma will later fall back, remotely from its original location); and lead to the formation of a hook and an open-field penetrating-region that shift in position.

4. Conclusion

We present a high-resolution observational case study of an anemone solar jet eruption associated with a circular flare ribbon. This event was analysed through coordinated observations obtained with SST, IRIS, and SDO, thus providing a clear picture of the low atmospheric signatures of a wide impulsive solar jet. Before and during the jet ejection, we classified three different phases of the jet: the quiet phase, the impulsive phase, and the recovery phase. The main finding of the present study is the presence of three peculiar features in the observations, specifically a hook formation along the circular flare ribbon, a gradual widening of the jet through the motion of its kinked edge towards the magnetic reconnection site, and the falling back of some of the jet plasma at a different location than its launching site.

The observed parasitic magnetic field topology (concentrated positive polarity surrounded by scattered negative polarity) and the $H\alpha$ observations with a wide and impulsive jet show a similarity with the model given by [Pariat et al. \(2015\)](#) using the ARMS simulation. Therefore, we compared the above-identified features with this numerical simulation. The results of the model from the ARMS simulation were analysed in detail to get a better understanding of the physics in comparison to the observations.

From the modelling point of view, the quiet-phase jet in the observation is explained as “early reconnection and straight jet” and regarded as a precursor of the upcoming dynamic jet. The impulsive phase in the observations is comparable with the model with the fast widening of the jet and a hook-like structure formation inside the circular ribbon. The recovery phase in the observations is illustrated in comparison to the model as the opening of a different set of magnetic field lines without putting any specific changes in the simulation. This has been noticed as an offset of the downflowing jet material from its launching site in the observations. This offset downflow of the jet plasma and the hook formation in the observations as well as in the models are linked through magnetic reconnection in the corona. The moving hook structure is the low atmospheric response to the coronal reconnection, which is evident since the reconnection process has closed the previously opened magnetic field lines from which the jet has an upflow. A different set of magnetic field lines were opened after reconnection, from which the jet material fell back to a different position as of its launch site. In short, this generic and non-specific simulation reproduces the very distinct behaviours that are present in the high-resolution

SST and IRIS observations. Furthermore, we regard it as likely that a model that incorporates chromospheric conditions will also explain the ejection of cool material, as the anemone-type structure is favourable for the ejection of cool jets.

In this study, we suggest that the components of the [Pariat et al. \(2015\)](#) model naturally give rise to the observed features while acknowledging the potential for alternative explanations from different numerical experiments (e.g., [Archontis & Hood 2013](#); [Wyper et al. 2017](#)). Here we explain the coherence between the observed characteristics and the pre-jet physical elements in the corona. We conjecture that the highly resolved observations of a swirled-anemone jet presented in this example likely reveal generic features inherent in wide and impulsive jets. We propose that their absence from earlier reports may be attributed to their potential blending with other features within more complex environments. Therefore, to detect and study such features, high-resolution observations of jets in both the solar corona and lower solar atmospheric layers using advanced imaging and spectroscopic techniques are necessary. Such observations can be obtained with the *Daniel K. Inouye* Solar Telescope (DKIST; [Rimmele et al. 2020](#)), the Solar-C (EUVST; [Shimizu et al. 2020](#)), the Multi-slit Solar Explorer (MUSE; [De Pontieu et al. 2022](#)), and the European Solar Telescope (EST; [Quintero Noda et al. 2022](#)).

Acknowledgements. We acknowledge the anonymous referee for the valuable comments and suggestions. This research has been supported by the Research Council of Norway, project number 325491, and through its Centres of Excellence scheme, project number 262622, by the European Research Council through the Synergy Grant number 810218 (“The Whole Sun”, ERC-2018-SyG), by the APR program of the French national space agency (CNES), and by the Programme National Soleil Terre (PNST) of the CNRS/INSU also co-funded by CNES and CEA. This work benefited from discussions at the International Space Science Institute (ISSI) in Bern, through project #535 “Unraveling surges: a joint perspective from numerical models, observations, and machine learning”. The Swedish 1-m Solar Telescope is operated on the island of La Palma by the Institute for Solar Physics of Stockholm University in the Spanish Observatorio del Roque de Los Muchachos of the Instituto de Astrofísica de Canarias. The Institute for Solar Physics is supported by a grant for research infrastructures of national importance from the Swedish Research Council (registration number 2017-00625). SDO observations are courtesy of NASA/SDO and the AIA, EVE, and HMI science teams. IRIS is a NASA small explorer mission developed and operated by LMSAL with mission operations executed at NASA Ames Research center and major contributions to downlink communications funded by ESA and the Norwegian Space Agency. The numerical simulations were carried on the HPC resources of the National Computer Center for Higher Education (CINES), through time allocation A0010406331 granted by Grand Équipement National de Calcul Intensif (GENCI). This project was also provided with computer and storage resources by GENCI at IDRIS thanks to the grant A0130406331 on the supercomputer Jean Zay’s the CSL partition. We made use of NASA’s Astrophysics Data System Bibliographic Service. We thank to Dr. Valentin Aslanyan for making available his QSL computation routines.

References

- Archontis, V., & Hood, A. W. 2013, *ApJ*, **769**, L21
 Aslanyan, V., Pontin, D. I., Wyper, P. F., et al. 2021, *ApJ*, **909**, 10
 Aulanier, G., & Dudík, J. 2019, *A&A*, **621**, A72
 Carlsson, M., Leenaarts, J., & De Pontieu, B. 2015, *ApJ*, **809**, L30
 Chen, F., Rempel, M., & Fan, Y. 2022, *ApJ*, **937**, 91
 Cheng, X., Priest, E. R., Li, H. T., et al. 2023, *Nat. Commun.*, **14**, 2107
 Chifor, C., Isobe, H., Mason, H. E., et al. 2008, *A&A*, **491**, 279
 Cirtain, J. W., Golub, L., Lundquist, L., et al. 2007, *Science*, **318**, 1580
 Dalmasse, K., Pariat, E., Antiochos, S. K., & DeVore, C. R. 2012, in *EAS Publications Series*, eds. M. Fauroubert, C. Fang, & T. Corbard, 55, 201
 de la Cruz Rodríguez, J., Löfdahl, M. G., Sütterlin, P., Hillberg, T., & Rouppe van der Voort, L. 2015, *A&A*, **573**, A40
 De Pontieu, B., Title, A. M., Lemen, J. R., et al. 2014, *Sol. Phys.*, **289**, 2733
 De Pontieu, B., Testa, P., Martínez-Sykora, J., et al. 2022, *ApJ*, **926**, 52
 Démoulin, P., Henoux, J. C., Priest, E. R., & Mandrini, C. H. 1996, *A&A*, **308**, 643
 Devi, P., Joshi, B., Chandra, R., et al. 2020, *Sol. Phys.*, **295**, 75
 DeVore, C. R. 1991, *J. Comput. Phys.*, **92**, 142
 Fang, F., Fan, Y., & McIntosh, S. W. 2014, *ApJ*, **789**, L19
 González-Avilés, J. J., Guzmán, F. S., Fedun, V., & Verth, G. 2020, *ApJ*, **897**, 153
 Guglielmino, S. L., Bellot Rubio, L. R., Zuccarello, F., et al. 2010, *ApJ*, **724**, 1083
 Heyvaerts, J., Priest, E. R., & Rust, D. M. 1977, *ApJ*, **216**, 123
 Howard, R. A., Moses, J. D., Vourlidas, A., et al. 2008, *Space Sci. Rev.*, **136**, 67
 Joshi, R., Schmieder, B., Chandra, R., et al. 2017, *Sol. Phys.*, **292**, 152
 Joshi, R., Chandra, R., Schmieder, B., et al. 2020a, *A&A*, **639**, A22
 Joshi, R., Schmieder, B., Aulanier, G., Bommier, V., & Chandra, R. 2020b, *A&A*, **642**, A169
 Joshi, R., Schmieder, B., Heinzl, P., et al. 2021, *A&A*, **654**, A31
 Karpen, J. T., Antiochos, S. K., & DeVore, C. R. 2012, *ApJ*, **760**, 81
 Karpen, J. T., DeVore, C. R., Antiochos, S. K., & Pariat, E. 2017, *ApJ*, **834**, 62
 Lemen, J. R., Title, A. M., Akin, D. J., et al. 2012, *Sol. Phys.*, **275**, 17
 Mandrini, C. H., Démoulin, P., Schmieder, B., Deng, Y. Y., & Rudawy, P. 2002, *A&A*, **391**, 317
 Masson, S., Pariat, E., Aulanier, G., & Schrijver, C. J. 2009, *ApJ*, **700**, 559
 Moore, R. L., Cirtain, J. W., Sterling, A. C., & Falconer, D. A. 2010, *ApJ*, **720**, 757
 Moreno-Insertis, F., & Galsgaard, K. 2013, *ApJ*, **771**, 20
 Moreno-Insertis, F., Galsgaard, K., & Ugarte-Urra, I. 2008, *ApJ*, **673**, L211
 Nishizuka, N., Nakamura, T., Kawate, T., Singh, K. A. P., & Shibata, K. 2011, *ApJ*, **731**, 43
 Nóbrega-Siverio, D., Moreno-Insertis, F., & Martínez-Sykora, J. 2016, *ApJ*, **822**, 18
 Nóbrega-Siverio, D., Martínez-Sykora, J., Moreno-Insertis, F., & Rouppe van der Voort, L. 2017, *ApJ*, **850**, 153
 Nóbrega-Siverio, D., Moreno-Insertis, F., Galsgaard, K., et al. 2023, *ApJ*, **958**, L38
 Pariat, E., Antiochos, S. K., & DeVore, C. R. 2009, *ApJ*, **691**, 61
 Pariat, E., Antiochos, S. K., & DeVore, C. R. 2010, *ApJ*, **714**, 1762
 Pariat, E., Dalmasse, K., DeVore, C. R., Antiochos, S. K., & Karpen, J. T. 2015, *A&A*, **573**, A130
 Pariat, E., Dalmasse, K., DeVore, C. R., Antiochos, S. K., & Karpen, J. T. 2016, *A&A*, **596**, A36
 Patsourakos, S., Pariat, E., Vourlidas, A., Antiochos, S. K., & Wuelser, J. P. 2008, *ApJ*, **680**, L73
 Pesnell, W. D., Thompson, B. J., & Chamberlin, P. C. 2012, *Sol. Phys.*, **275**, 3
 Prasad, A., Dissauer, K., Hu, Q., et al. 2020, *ApJ*, **903**, 129
 Quintero Noda, C., Schlichenmaier, R., Bellot Rubio, L. R., et al. 2022, *A&A*, **666**, A21
 Raouafi, N. E., Patsourakos, S., Pariat, E., et al. 2016, *Space Sci. Rev.*, **201**, 1
 Rimmele, T. R., Warner, M., Keil, S. L., et al. 2020, *Sol. Phys.*, **295**, 172
 Rouppe van der Voort, L. H. M., De Pontieu, B., Carlsson, M., et al. 2020, *A&A*, **641**, A146
 Savcheva, A., Pariat, E., McKillop, S., et al. 2015, *ApJ*, **810**, 96
 Savcheva, A., Pariat, E., McKillop, S., et al. 2016, *ApJ*, **817**, 43
 Scharmer, G. B., Bjelksjo, K., Korhonen, T. K., Lindberg, B., & Petterson, B. 2003, in *Innovative Telescopes and Instrumentation for Solar Astrophysics*, eds. S. L. Keil, & S. V. Avakyan, *SPIE Conf. Ser.*, **4853**, 341
 Scharmer, G. B., Narayan, G., Hillberg, T., et al. 2008, *ApJ*, **689**, L69
 Schmieder, B., Mein, P., Vial, J.-C., & Tandberg-Hanssen, E. 1983, *A&A*, **127**, 337
 Schmieder, B., Shibata, K., van Driel-Gesztelyi, L., & Freeland, S. 1995, *Sol. Phys.*, **156**, 245
 Schmieder, B., Joshi, R., & Chandra, R. 2022, *Adv. Space Res.*, **70**, 1580
 Schou, J., Scherrer, P. H., Bush, R. I., et al. 2012, *Sol. Phys.*, **275**, 229
 Scott, R. B., Bradshaw, S. J., & Linton, M. G. 2022, *ApJ*, **933**, 72
 Shen, Y. 2021, *Proc. R. Soc. London Ser. A*, **477**, 217
 Shibata, K., Nozawa, S., & Matsumoto, R. 1992, *PASJ*, **44**, 265
 Shibata, K., Masuda, S., Shimojo, M., et al. 1995, *ApJ*, **451**, L83
 Shibata, K., Yokoyama, T., & Shimojo, M. 1996, *J. Geomagn. Geoelectr.*, **48**, 19
 Shibata, K., Nakamura, T., Matsumoto, T., et al. 2007, *Science*, **318**, 1591
 Shimizu, T., Imada, S., Kawate, T., et al. 2020, *SPIE Conf. Ser.*, **11444**, 114440N
 Shimojo, M., & Shibata, K. 2000, *ApJ*, **542**, 1100
 Singh, K. A. P., Isobe, H., Nishizuka, N., Nishida, K., & Shibata, K. 2012, *ApJ*, **759**, 33
 Skogsrud, H., Rouppe van der Voort, L., & De Pontieu, B. 2016, *ApJ*, **817**, 124
 Sterling, A. C., Moore, R. L., & Panesar, N. K. 2018, *ApJ*, **864**, 68
 Tassev, S., & Savcheva, A. 2017, *ApJ*, **840**, 89
 Titov, V. S. 2007, *ApJ*, **660**, 863
 Titov, V. S., Hornig, G., & Démoulin, P. 2002, *J. Geophys. Res.: Space Phys.*, **107**, 1164
 Titov, V. S., Mikić, Z., Linker, J. A., Lionello, R., & Antiochos, S. K. 2011, *ApJ*, **731**, 111

- Török, T., Aulanier, G., Schmieder, B., Reeves, K. K., & Golub, L. 2009, [ApJ](#), **704**, 485
- Uddin, W., Schmieder, B., Chandra, R., et al. 2012, [ApJ](#), **752**, 70
- Van Noort, M., Rouppe Van Der Voort, L., & Löfdahl, M. G. 2005, [Sol. Phys.](#), **228**, 191
- Wyper, P. F., & DeVore, C. R. 2016, [ApJ](#), **820**, 77
- Wyper, P. F., DeVore, C. R., Karpen, J. T., & Lynch, B. J. 2016, [ApJ](#), **827**, 4
- Wyper, P. F., Antiochos, S. K., & DeVore, C. R. 2017, [Nature](#), **544**, 452
- Wyper, P. F., DeVore, C. R., & Antiochos, S. K. 2018, [ApJ](#), **852**, 98
- Wyper, P. F., DeVore, C. R., & Antiochos, S. K. 2019, [MNRAS](#), **490**, 3679
- Yokoyama, T., & Shibata, K. 1995, [Nature](#), **375**, 42
- Yokoyama, T., & Shibata, K. 1996, [Astrophys. Lett. Commun.](#), **34**, 133
- Zhang, Q. M., Chen, P. F., Guo, Y., Fang, C., & Ding, M. D. 2012, [ApJ](#), **746**, 19
- Zuccarello, F. P., Chandra, R., Schmieder, B., Aulanier, G., & Joshi, R. 2017, [A&A](#), **601**, A26